The nonlinear dispersion relation of geodesic acoustic modes

Robert Hager and Klaus Hallatschek

View Online   Export Citation   CrossMark

ARTICLES YOU MAY BE INTERESTED IN
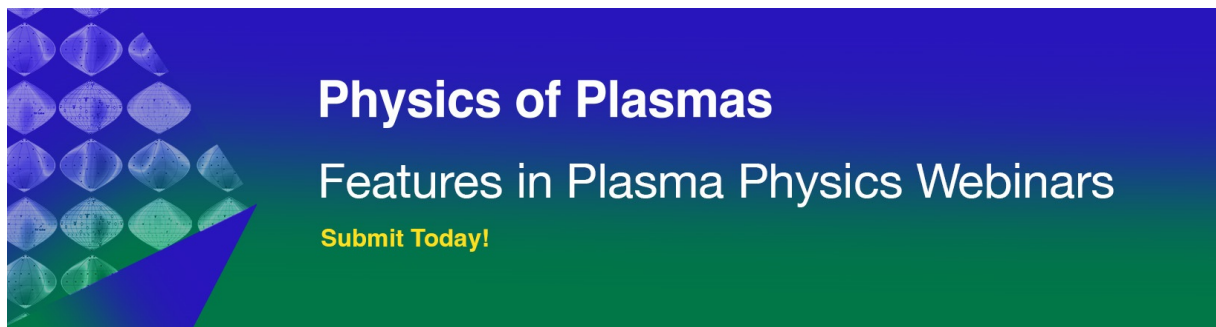
Physics of Plasmas

Features in Plasma Physics Webinars

Submit Today!

AIP Publishing

The nonlinear dispersion relation of geodesic acoustic modes

Robert Hager[a)] and Klaus Hallatschek[b)]

Max-Planck-Institut für Plasmaphysik Boltzmannstraße 2, D-85748 Garching, Germany

The energy input and frequency shift of geodesic acoustic modes (GAMs) due to turbulence in tokamak edge plasmas are investigated in numerical two-fluid turbulence studies. Surprisingly, the turbulent GAM dispersion relation is qualitatively equivalent to the linear GAM dispersion but can have drastically enhanced group velocities. As a consequence radially broad ($\sim$cm) GAM eigenmodes may form. Those may lead to experimentally observable deviations from the expected scaling of the GAM frequency with the square root of the plasma temperature. In up-down asymmetric geometry, the energy input due to turbulent transport may favor the excitation of GAMs with one particular sign of the radial phase velocity relative to the magnetic drifts. Including the radial gradient of the GAM frequency may lead to periodic bursts of the GAM and the turbulence intensity.
[http://dx.doi.org/10.1063/1.4747725]

I. INTRODUCTION

Geodesic acoustic modes (GAMs), oscillating plasma flows associated with radial gradients of the electrostatic potential,[1] are a frequent phenomenon in tokamak edge plasmas.[2] The interplay between GAMs and the quasi-two dimensional turbulence, which is typically generated by variations of the Rayleigh-Taylor instability, is particularly interesting. Different aspects of the GAM-turbulence interaction were studied in Refs. 3–8. By shearing the turbulence, GAMs are able to modulate the turbulent transport and to reduce the saturation intensity of the turbulence.[9] The present article is an extension to our recently published Letter.[10] It features details of the calculations therein, which could not be included in the original publication, as well as some new insights.

Using numerical two-fluid turbulence studies with the code NLET,[11] we investigate both channels through which GAMs interact with the turbulence, energy input *and* frequency shift. In contrast to magnetohydrodynamics, the two-fluid description incorporates effects such as the generation of electric fields from electron pressure fluctuations and limited finite Larmor radius (FLR) effects (diamagnetic heat and momentum fluxes). Collisionless effects are only included in a very reduced form as effective dissipation coefficients. From the radial structure of global GAM eigenmodes[12] in non-local (non-Boussinesq) computations, we deduce a *nonlinear*, i.e., turbulence induced, dispersion relation. Although the observed dispersion agrees qualitatively with the ones obtained from linearized two-fluid equations,[13,14] the corresponding group velocities tend to be surprisingly high. For realistic edge parameters, the global eigenmodes have a radial extent of several centimeters and could account for the frequency plateaus in ASDEX Upgrade,[15,16] which deviate from the expected $T^{1/2}$ dependence of acoustic frequencies. If the equilibrium magnetic field is up-down asymmetric, we observe periodic bursts of turbulence and GAM activity. They can be traced back to an energy transfer from the turbulence

to the flows which is odd in the radial wavenumber and absent with symmetry. This behavior resembles strikingly the experimentally observed pulsation during the I phase in ASDEX Upgrade[2] or the periodic turbulence suppression in NSTX.[17] However, our turbulence computations aimed at the nonlinear effects induced by up-down asymmetry of the flux-surfaces and non-locality on the GAM rather than at a physically comprehensive simulation of the I phase.

The remainder of this article is organized as follows. In Sec. II, we derive time evolution equations of the GAM based on the two-fluid equations used in the code NLET. Furthermore, we briefly explain the computational setup of the discussed turbulence computations. Observations of turbulence induced shifts of the GAM frequency are discussed in Sec. III, and energy transfers between GAMs and the turbulence leading to pulsed GAM activity are analyzed in Sec. IV. Finally, we summarize and discuss our results in Sec. V.

II. BASIC EQUATIONS

For the numerical investigation presented here, we applied the Braginskii fluid code NLET.[11] A subset of the corresponding fluid equations are used to derive the time evolution equations for the $\boldsymbol{E} \times \boldsymbol{B}$ flow of the GAM and its pressure side-band. The resulting system of equations also provides the basis for the quantitative analysis of the GAM-turbulence interaction. In order to keep the discussion transparent, we restrict ourselves to the case of high safety factors q. In fact, this is hardly a restriction because the GAM is subject to enhanced Landau damping[18] and resonances with sound waves[13] for $q \lesssim 3$. On the contrary, for $q > 3$ finite q effects do not alter the (linear) GAM dynamics substantially as was shown by a comparison between two-fluid and gyro-kinetic theory in Ref. 13. The vorticity, the density, and the ion temperature equations for arbitrary flux surface shape and toroidal mode number $n = 0$ are given by[11]

$$\frac{|\nabla r|^2}{B^3} \partial_r \cdot \left[\frac{n}{\lambda} D_t \left(\partial_r \phi + \frac{\tau \alpha_d}{n} \partial_r p_i \right) \right] + \frac{C}{B\lambda} \partial_r p - \partial_\parallel \frac{j_\parallel}{B} = 0,$$

$$\tag{1}$$

$$\frac{D_t n}{B} - \frac{\epsilon_n C}{B} \frac{n}{\lambda} \left(\partial_r \phi - \frac{\alpha_d}{n} \partial_r p_e \right) - \alpha_d \epsilon_n (1+\tau) \partial_\parallel \frac{j_\parallel}{B} = 0, \quad (2)$$

$$\frac{D_t T_i}{B} - \frac{2}{3} \frac{\epsilon_n C}{B} \frac{T_i}{\lambda} \left(\partial_r \phi - \frac{\alpha_d}{n} \partial_r p_e + \frac{5}{2} \tau \alpha_d \partial_r T_i \right)$$
$$- \frac{2}{3} \kappa_i \partial_\parallel \left(\frac{T_i^{5/2}}{B \lambda} \partial_\parallel T_i \right) - \frac{2}{3} \epsilon_n \alpha_d (1+\tau) \frac{T_i}{n} \partial_\parallel \frac{j_\parallel}{B} = 0. \quad (3)$$

In these equations, ϕ is the electrostatic potential, n the density, $T_{i,e}$, and $p_{i,e} = n T_{i,e}$ the ion and electron temperature and pressure, $p = (p_e + \tau p_i)/(1+\tau)$ the total pressure, and $j_\parallel$ the parallel current density. Density and temperature are normalized to their values in the middle of the radial computational domain, i.e., $(n, T_{e/i}) \equiv \lambda(n_p, T_{p,e/i})/(n_{p,0}, T_{p,e/i,0})$, and $\tau \equiv T_{p,i,0}/T_{p,e,0}$. The potential is normalized as $\phi = \alpha_d \lambda(e\phi_p)/T_{p,e,0}$, where e is the elementary charge. Time and length are normalized to the resistive ballooning growth time t_{RB} and scale length L_{RB}, respectively (for definitions see Ref. 11). Apart from τ, the dimensionless parameters appearing in the equations are $\epsilon_n \equiv 2L_n/R_0$ with the density gradient length $L_n = 1/(\partial_r \ln n)$ and the major radius at the outer midplane R_0. α_d is the ratio of the drift frequency to the ballooning growth rate and $\lambda^{-1} \equiv L_{RB}/L_n \propto \rho^\star$ is the ratio of the turbulence- to the background scale lengths. (A ratio of $\lambda \sim 1 - 50$ is typical for the edge region.) Note that the subset of the fluid equations used in NLET presented here is for isothermal electrons, high safety factors ($\epsilon_v = 0$), and neglects magnetic pumping ($\gamma_p = 0$). The radial coordinate r is a flux surface label, namely the minor radial excursion from the outermost point of a reference flux surface marked with $r = 0$. The varying differential flux surface distance is accounted for by $|\nabla r|$. B is the magnetic field normalized to its value at the outer midplane and D_t is the convective time derivative $\partial_t + \boldsymbol{v}_E \cdot \nabla$ with $\boldsymbol{v}_E = \boldsymbol{b} \times \nabla \phi$ being the $\boldsymbol{E} \times \boldsymbol{B}$ drift at the outer midplane. The influence of the magnetic curvature is represented by the dimensionless function

$$C = C(\theta) \equiv \frac{R_0 |\nabla r|}{B} (\boldsymbol{b} \times \nabla \ln B) \cdot \hat{\boldsymbol{r}}, \quad (4)$$

which describes the curvature induced divergence of the $\boldsymbol{E} \times \boldsymbol{B}$-drift, i.e., $\nabla \cdot \boldsymbol{v}_{E,\theta} = C(\theta) \partial_r \phi$.

Flux-surface averages are defined as

$$\langle \ldots \rangle_p \equiv \frac{\oint \ldots B^{-1} dl_\parallel}{\oint B^{-1} dl_\parallel}, \quad \langle \ldots \rangle_v \equiv \frac{\oint \ldots |\nabla r|^2 B^{-3} dl_\parallel}{\oint |\nabla r|^2 B^{-3} dl_\parallel} \quad (5)$$

and $f_{av} \equiv \oint B^{-1} dl_\parallel / \oint |\nabla r|^2 / B^3 dl_\parallel$ with the parallel path length $dl_\parallel$.

A. GAM time evolution

For the derivation of the GAM time evolution equations, we prefer to normalize length to the sound gyro radius $\rho_s \equiv (m_i(T_{p,e,0} + \gamma T_{p,i,0}))^{1/2}/(eB_p)$ and time to $t_0 = R_{eff}/(\sqrt{2}c_s)$, where $c_s \equiv ((T_{e,p,0} + \gamma T_{i,p,0})/m_i)^{1/2}$ is the sound speed for isothermal electrons, m_i is the ion mass, B_p the magnetic

field (in physical units), $\gamma = 5/3$ the adiabatic exponent, and $1/R_{eff} \equiv (2\langle C(\theta)^2 \rangle f_{av})^{1/2}/R_0$. In these units, the GAM frequency at $k_r = 0$ and $r = 0$ is one ($\omega_{GAM,0}(r=0) = 1$). The potential ϕ is normalized to $T_{i,p,0} + T_{e,p,0}$ instead of just $T_{e,p,0}$. In order to retain non-local effects while preventing transitions between regions dominated by different types of turbulence and keeping the discussion transparent, we assume mild non-locality. Thus, we approximate $D_t p \approx n_b D_t T_i + T_{i,b} D_t n$ and $n D_t \partial_r \phi \approx n_b D_t \partial_r \phi$, where the subscript "b" denotes a background quantity. In the actual numerical analysis in Secs. III and IV, the evolution of the background density and temperature are retained. Finally, the $(m=0, n=0)$ component of the potential (providing the flow component of the GAM) is separated from the components with higher m by defining $\phi = \phi_0(r) + \tilde{\phi}$.

Using the conventions and definitions given above, the derivation of the system of equations describing the time evolution of the GAM from Eqs. (1)–(3) is straightforward. The equation for the flow is given by

$$\partial_t \left(\sqrt{\frac{f_T}{f_{T,0} f_{av}}} n_b \partial_r \phi_0 \right) = -\sqrt{\frac{f_T}{f_{T,0}}} \left\langle \tilde{C} p \right\rangle_p$$
$$- \sqrt{\frac{f_T}{f_{T,0} f_{av}}} \partial_t \left\langle n_b \partial_r \tilde{\phi} + \alpha_\tau \partial_r p_i \right\rangle_v$$
$$- \sqrt{\frac{f_T}{f_{T,0} f_{av}}} n_b \partial_r$$
$$\times \left\langle v_{E,r} \left(\partial_r \phi + \alpha_\tau \frac{\partial_r p_i}{n_b} \right) \right\rangle_v, \quad (6)$$

and the equation for the pressure sideband $\langle \tilde{C} p \rangle_p$ by

$$\partial_t \langle \tilde{C} p \rangle_p = \sqrt{\frac{f_T}{f_{T,0}}} \left(\sqrt{\frac{f_T}{f_{T,0} f_{av}}} n_b \partial_r \phi_0 \right) - \partial_r \left\langle \tilde{C} v_{E,r} p \right\rangle_p$$
$$+ \frac{f_T}{f_{T,0} \sqrt{f_{av}}} \left\langle \tilde{C}^2 [n_b \partial_r \tilde{\phi} + \alpha_\tau (\partial_r p_i + \beta_\tau \lambda^{-1} n_b T_{i,b} \partial_r T_i)] \right\rangle_p, \quad (7)$$

where $\alpha_\tau \equiv \tau/(1+\tau)$, $\beta_\tau = \gamma\tau/(1+\gamma\tau)$. Here, we have dropped terms of order $(k_r \rho_s)^3$ in Eq. (7) and abbreviated $\tilde{C} \equiv C/\langle C^2 \rangle^{1/2}$. The variation of the background temperatures is expressed by $f_T \equiv \lambda^{-1}(T_{e,b} + \gamma T_{i,b})/(1+\tau)$ and $f_{T,0} \equiv (1+\gamma\tau)/(1+\tau)$. We can express this in a simplified notation as

$$\partial_t p_{GAM} = v_{GAM} + s_\Gamma + s_{dia,p}, \quad (8)$$

$$\partial_t v_{GAM} = -p_{GAM} + s_\Pi + s_{dia,\phi}, \quad (9)$$

where the various terms denoted s_x on the right hand side describe the nonlinear and FLR effects on the GAM, whereas v_{GAM} and p_{GAM} describe the linear time evolution for $k_r = 0$. The definitions used in Eqs. (8) and (9) are

$$p_{GAM} \equiv \left\langle \tilde{C} \sqrt{\frac{f_{T_0}}{f_T}} p \right\rangle_p,$$

$$v_{GAM} \equiv \sqrt{\frac{f_T}{f_{T_0} f_{av}}} n_b \partial_r \phi_0,$$

$$s_\Gamma \equiv -\partial_r \left\langle \tilde{C} v_{E,r} \sqrt{\frac{f_{T_0}}{f_T}} p \right\rangle_p \equiv -\partial_r \Gamma_{p,a},$$

$$s_{dia,p} \equiv \sqrt{\frac{f_T}{f_{T_0} f_{av}}} n_b \left\langle \tilde{C}^2 \left[\partial_r \tilde{\phi} + \alpha_\tau \left(\frac{\partial_r p_i}{n_b} + \beta_\tau \partial_r T_i \right) \right] \right\rangle_p,$$

$$s_\Pi \equiv -\sqrt{\frac{f_T}{f_{T_0} f_{av}}} n_b \partial_r \left\langle v_{E,r} \left(\partial_r \phi + \alpha_\tau \frac{\partial_r p_i}{n_b} \right) \right\rangle_v,$$

$$s_{dia,\phi} \equiv -\sqrt{\frac{f_T}{f_{T_0} f_{av}}} n_b \partial_t \left\langle \partial_r \tilde{\phi} + \alpha_\tau \frac{\partial_r p_i}{n_b} \right\rangle_v. \tag{10}$$

In the oscillator equations (8) and (9), p_{GAM} has the role of the potential energy, v_{GAM} is the angular momentum, s_Γ and s_Π are the divergences of the turbulent transport and the Reynolds stress. The terms denoted s_{dia} represent the coupling between the GAM pressure and flow components to the diamagnetic drift of the plasma. Defining the current state of the GAM as a vector $\mathbf{\Psi} \equiv (p_{GAM}, v_{GAM})$ in the pressure-velocity plane, Eqs. (8) and (9) can be written as

$$\partial_t \mathbf{\Psi} = \delta \mathbf{\Psi}_{lin} + \delta \mathbf{\Psi}_{nl}, \tag{11}$$

where $\delta \mathbf{\Psi}_{lin} \equiv (v_{GAM}, -p_{GAM})$ and $\delta \mathbf{\Psi}_{nl} \equiv (s_\Gamma + s_{dia,p}, s_\Pi + s_{dia,\phi})$. The energy stored in the GAM corresponds to the squared length of the state vector $\mathbf{\Psi}$. In the limit $k_r \to 0$, the source terms on the right hand side of Eq. (11) vanish. In this framework, the remaining linear oscillation (at constant GAM energy) corresponds to a circular rotation of the tip of the vector $\mathbf{\Psi}$ around the origin at the GAM frequency $\omega_{GAM,0}(r=0)$ because obviously $\mathbf{\Psi} \cdot \delta \mathbf{\Psi}_{lin} = 0$. In contrast, the vector $\delta \mathbf{\Psi}_{nl}$ containing the nonlinear and FLR terms can have components parallel and orthogonal to $\mathbf{\Psi}$. The former correspond to an energy transfer between the turbulence and the GAM, whereas the latter correspond to a turbulence (or FLR) induced shift of the GAM phase, i.e., a frequency shift. With the basis vectors $\hat{\mathbf{e}}_\varphi \equiv \mathbf{\Psi}/|\mathbf{\Psi}|$ and $\hat{\mathbf{e}}_E \equiv \delta \mathbf{\Psi}_{lin}/|\delta \mathbf{\Psi}_{lin}|$, one obtains the frequency shift and the energy increment per time step

$$\delta \omega = \left\langle \frac{1}{|\mathbf{\Psi}|} \delta \mathbf{\Psi}_{nl} \cdot \hat{\mathbf{e}}_\varphi \right\rangle_t, \quad \frac{\delta E}{\delta t} = (\delta \mathbf{\Psi}_{nl} \cdot \hat{\mathbf{e}}_E)^2, \tag{12}$$

where $\langle \ldots \rangle_t$ indicates time averaging.

The method introduced above will be applied in quantitative analyses of the GAM-turbulence interaction in numerical turbulence computations in the remainder of this article.

B. Computational setup

We briefly summarize the basic computational setup of the turbulence runs discussed in Secs. III–V. The computational domain covers $150 L_0$ (≈ 580 sound gyro radii) radially and poloidally. To avoid effects induced by the boundary conditions, we use an effective radial domain of $490\rho_s$. Furthermore, we choose $\eta_i \equiv L_n/L_{T_i} = 2.4$, $\eta_e \equiv L_n/L_{T_e} = 0$, $\epsilon_n = 0.05$, $\alpha_d = 0.5$, and $\partial \ln q/\partial \ln r = 1$. The electrons are isothermal and treated non-adiabatically. The background density and temperature profiles are linear, $n_b = \lambda - r$ and $T_{i,b} = \lambda - 2.4r$. Thus, the local GAM frequency at zero radial wave number $\omega_{GAM,0}(r)$ varies by roughly $\pm 0.3 \omega_{GAM,0}(r=0)$.

III. NONLINEAR GAM DISPERSION

Figure 1 shows the result of a nonlocal ($\lambda \approx 200$) ion temperature gradient (ITG) driven turbulence computation with circular flux surfaces, which displays pronounced GAM activity. The radial variation of the GAM frequency caused by non-locality is obvious in the corresponding $\mathbf{E} \times \mathbf{B}$-flow profile [Fig. 1(a)]. Its temporal Fourier transform [Fig. 1(b)] reveals that GAMs with frequency $\omega_{GAM,0}(r_0)$ (indicated by the dashed line) radiate significantly outwards to $r > r_0$ but disappear for $r < r_0$. The deviations from the local GAM frequency reach up to 30%. The application of a narrow band
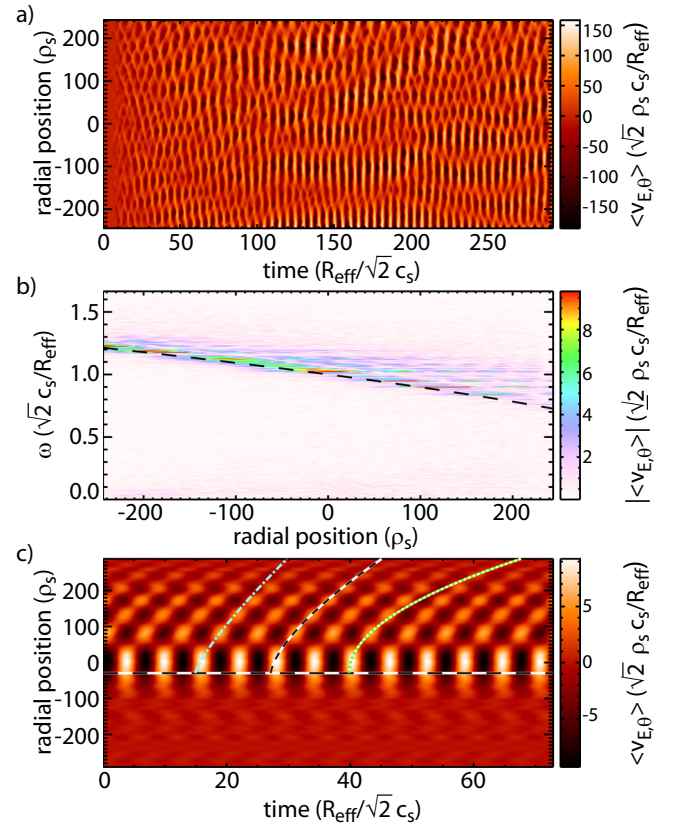

FIG. 1. Results of a non-local NLET turbulence study with slow parameter variation, $\lambda \approx 200$. (a) Flux-surface averaged poloidal $\mathbf{E} \times \mathbf{B}$ velocity $\langle v_{E,\theta} \rangle$. (b) Temporal Fourier transform (linear color scale, truncated at 60% of the intensity maximum) of (a) with the local GAM frequency indicated by the dashed line. (c) Band-pass filtered flow profile at $\omega = \omega_{GAM,0}(r_0) = 1.03$ with fits to curves of constant phase according to Eq. (15) with $\beta = 4$ (dashed-dotted), $\beta = 2$ (dashed), and $\beta = 1$ (dotted). Reference radius r_0 indicated by horizontal dashed line. Reprinted with permission from R. Hager and K. Hallatschek, Phys. Rev. Lett. **108**, 035004 (2012). Copyright © 2012 American Physical Society.

pass filter [Fig. 1(c)] shows that the flow profile consists of *global* GAM eigenmodes. The regular radial structure of this mode conveys much information. The standing wave pattern emerges from the interference between an incoming and a reflected GAM. The reflection occurs where the frequency of the eigenmode is equal to the GAM frequency at $k_r = 0$, i.e., at $r = r_0$. The radial scale length of the eigenmode—visible as the slope of the curves on which the GAM phase is constant—depends on the radial position, or to be precise, on the background temperature. We assume for now that the GAM in Fig. 1(b) can be described by a dispersion relation $\omega(r, k_r)$. Consequently, the dispersion relation of the GAM must be symmetric with respect to $k_r = 0$. Otherwise, the phase velocities of incoming and reflected wave would differ and one could only observe traveling waves. Finally, the fact that GAM activity is observed only outside the cut-off layer $r = r_0$ reveals that group and phase velocity must be in the same direction, i.e. the dispersion has a minimum at $k_r = 0$.

We describe such an eigenmode by a WKB wave packet with a local wave number k_r obeying $\omega_{GAM}(r, k_r) = const$. To relate the observed deviations from $\omega_{GAM,0}(r_0)$ to the nonlinear GAM properties, we choose the Ansatz

$$\omega_{GAM}(r, k_r) = \omega_{GAM,0}(r)\left(1 + \alpha|k_r|^\beta\right) \qquad (13)$$

with a natural number β for the dispersion relation. The resulting solution for $|k_r|$ is

$$|k_r(r)| \approx \left[-\frac{1}{\alpha L_\omega}(r - r_0)\right]^{1/\beta}, \qquad (14)$$

where $L_\omega \equiv (\partial_r \ln \omega_{GAM,0})(r_0)$. Depending on the sign of α, $|k_r|$ has a solution on only one side of the flux surface $r = r_0$. $|k_r(r_0)| = 0$ implies the existence of a reflection layer at r_0. Using Eq. (14) and the condition $\dot{r} = \omega_{GAM,0}(r_0)/k_r$ for the phase velocity yields the curve of constant phase

$$t(r) = \frac{1}{1 + \frac{1}{\beta}}\left(-\frac{1}{\alpha L_\omega}\right)^{\frac{1}{\beta}}\frac{(r - r_0)^{1+\frac{1}{\beta}}}{\omega_{GAM,0}(r_0)} + t_0. \qquad (15)$$

The results of fits using Eq. (15) with different values of β for the band-pass filtered flow profile are shown in Fig. 1(c) with $\omega_{GAM,0}(r_0) = 1.03$. The best fit is obtained for $\beta = 2$. It yields $\alpha \approx 39\rho_s^2$, roughly a hundred times the value observed in the absence of turbulence ($|\alpha| \sim \rho_s^2/2$).[13] A comparison with the corresponding local run in Fig. 2(a) confirms the obtained dispersion relation as well as the conjectures on its properties stated before.

The above values for α can be used to estimate the radial extent of a global eigenmode whose radial structure is on the one hand given by an Airy function.[12] On the other hand the turbulence excites GAMs only in a limited range of radial wave numbers, whose distribution is assumed to be a Gaussian of width σ_k centered at $k_r = k_0$. Since the Airy function $\text{Ai}(x)$ drops only as $x^{1/4}$, the wave number distribution represents the dominant limitation of the mode
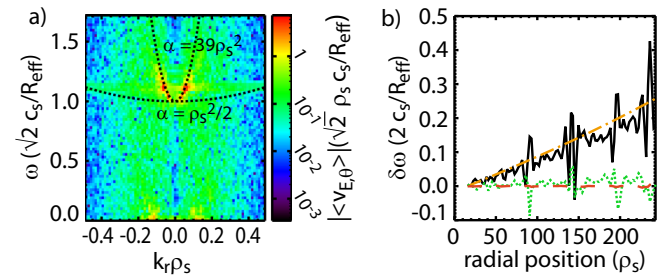

FIG. 2. (a) Spectrum of the flux-surface averaged poloidal $\mathbf{E} \times \mathbf{B}$ velocity $|\langle v_{E,\theta}\rangle|$ (logarithmic color scale) of a local NLET turbulence study otherwise equivalent to the one shown in Fig. 1 (using the parameters at $r = 0$) and dispersion relations $\omega_{GAM}(r, k_r) = \omega_{GAM,0}(r)(1 + \alpha|k_r|^2)$ with $\alpha = \rho_s^2/2$ (linear dispersion) and $\alpha = 39\rho_s^2$. (b) Nonlinear frequency shifts due to the couplings between turbulence and GAMs for the Fourier mode $\omega = 1.03$ of Fig. 1(a) frequency shift necessary for the radial mode structure in Fig. 1(c) (dashed-dotted), shift due to the up-down asymmetric component of the turbulent transport (solid), the Reynolds stress (dotted), and the diamagnetic velocity (dashed). Reprinted with permission from R. Hager and K. Hallatschek, Phys. Rev. Lett. **108**, 035004 (2012). Copyright © 2012 American Physical Society.

width. The estimate resulting from Eq. (14) is therefore $\delta r \lesssim 4\alpha L_\omega \sigma_k k_0$. On a basis of many turbulence computations, we choose $k_0\rho_s \sim 0.1$ and $\sigma_k\rho_s \sim 0.05$. In tokamak edge plasmas, $L_\omega \sim L_T \sim 0.01...0.1R$. Thus, assuming a major radius of $R \sim 1$ m, we obtain mode widths of $\delta r \lesssim 0.1 ...1$ mm, i.e., of the order of the gyro radius for $\alpha = \rho_s^2/2$. In contrast, for $\alpha = 39\rho_s^2$ $\delta r \lesssim 0.8...8$ cm. The corresponding group velocities are of the order of the ion magnetic drifts and the diamagnetic drift, respectively. Therefore, the width of nonlinear eigenmodes can be comparable to the scale length of the frequency plateaus reported in Ref. 15.

Now, we develop an understanding of the turbulence induced frequency shift by analyzing the GAM-turbulence interaction as described in Sec. II A. Splitting the nonlinear terms for the Fourier mode with $\omega = 1.03$ [Fig. 1(c)] into energy inputs and frequency shifts, we find that the observed frequency shift is due to the coupling to the up-down asymmetric component of the turbulent transport s_Γ alone, while the Reynolds stress and the diamagnetic terms do not contribute [Fig. 2(b)]. The diamagnetic term in the equation for the GAM flow velocity is small and not included in the figure. A reduction of the resistivity towards adiabaticity results in reduced GAM group velocities, indicating a strong dependence of this effect on the ballooning character of the turbulence. A turbulence computation with the gyrokinetic code gyro[19] with parameters equivalent to those of the adiabatic two-fluid computation even resulted in a GAM intensity spectrum which could readily be explained by the linear gyrokinetic GAM dispersion as given in Ref. 13.

Assuming positive phase velocity, the increase of the GAM frequency (and the phase velocity) due to the asymmetric transport requires the transport $\Gamma_{p,a} \equiv \langle Cv_{E,r}p\rangle_p$ to be in phase with p_{GAM} or equivalently the divergence of the transport to be in phase with v_{GAM} (Fig. 3). This conjecture can be verified applying a 2D cross correlation analysis with the normalized cross correlation defined as
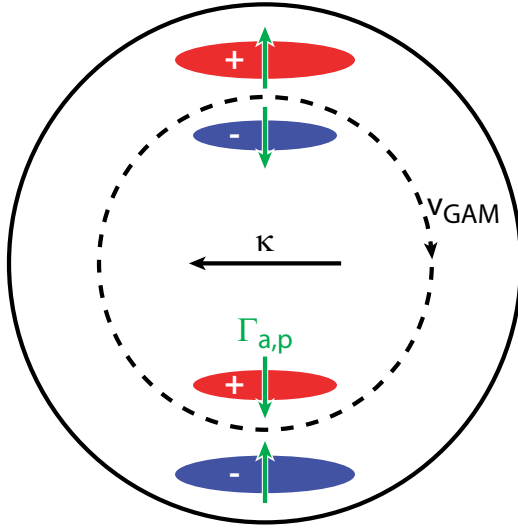
FIG. 3. Poloidal cross section of a tokamak with the curvature κ directed to the left. Illustration of a GAM with positive phase velocity (radially outward). The GAM induced pressure fluctuations p_{GAM} are indicated by the red $(+)$ and blue $(-)$ bubbles. If the up-down antisymmetric pressure transport $\Gamma_{a,p}$ (green arrows) is in phase with p_{GAM}, the transport supports the compression/expansion of the plasma due to the poloidal flow v_{GAM}, and increases the phase velocity, i.e., the frequency of the GAM.

$$\langle f(r,t), g(r,t)\rangle_{cc}(\delta r, \delta t)$$

$$\equiv \frac{\iint (f(r,t)-\bar{f})(g(r+\delta r, t+\delta t)-\bar{g})\mathrm{d}r\mathrm{d}t}{\sqrt{\left(\iint (f(r,t)-\bar{f})^2\mathrm{d}r\mathrm{d}t\right)\left(\iint (g(r,t)-\bar{g})^2\mathrm{d}r\mathrm{d}t\right)}}.$$

(16)

Figures 4(a) and 4(b) show the cross correlation $\langle p_{GAM}, \Gamma_{p,a}\rangle_{cc}$ (positive phase velocity components) for a nonadiabatic and an adiabatic local $(\lambda = 10^5)$ ITG turbulence computation, respectively. The parameters differ slightly from those of the computation discussed before. The parallel velocity is included by setting $\epsilon_v = 5.95 \times 10^{-3} \Longleftrightarrow q = 3$. Moreover, $\eta_i = 6.0$, and the domain size is $50L_0$ in the radial and poloidal direction. In the nonadiabatic case, p_{GAM} and $\Gamma_{p,a}$ are, indeed, correlated relatively well reflected by a correlation of about 0.45 at zero temporal and spatial
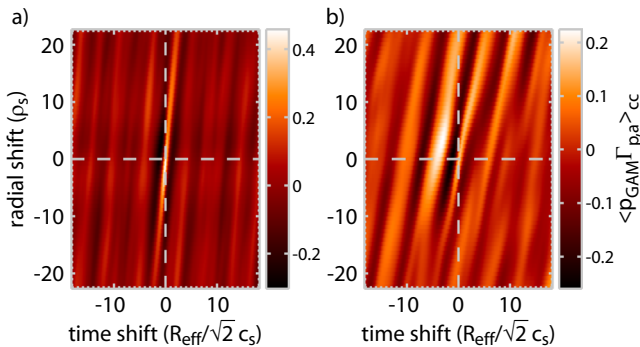

FIG. 4. 2D cross correlation between the positive phase velocity components of the GAM induced pressure perturbations and the up-down antisymmetric turbulent pressure transport, $\langle p_{GAM}\Gamma_{a,p}\rangle_c c$ for (a) nonadiabatic electron response and (b) adiabatic electrons.

shift. In the adiabatic case, this correlation drops to roughly one half the nonadiabatic value. In order to find the reason for this difference, we performed a series of NLET turbulence runs with the parameters described before, however, with varying parallel resistivity. This is achieved by varying the parameter α_d, which is inversely proportional to the square root of the parallel resistivity.[11] Taking the resistivity η in the reference run with $\alpha_d = 0.5$ to be η_0, the parameter scan with $0.35 \leq \alpha_d \leq 7$ reaches from $\eta/\eta_0 = 2$ to $\eta/\eta_0 = 5.1 \cdot 10^{-3}$. As a result of the increasing adiabaticity of the system, the cross correlation between p_{GAM} and $\Gamma_{p_{GAM}}$ drops surprisingly fast between $\alpha_d = 1$ and $\alpha_d = 1.5$ (Fig. 5). At higher values of α_d, the cross correlation remains roughly constant. A plot of $\langle p_{GAM}\Gamma_{p,a}\rangle$ against the resistivity (inset of Fig. 5) suggests that the correlation also saturates for $\alpha_d < 1$. However, another transition might occur for $\alpha_d < 0.35$, which is currently being checked in corresponding turbulence computations. The parameters used in our numerical studies, support our initial conjecture that the observed GAM behavior may be caused by a transition from resistive ballooning to ITG dominated turbulence.[11,20] A detailed study to test this hypothesis is under way.

IV. PULSED GAM ACTIVITY

We investigate the effect of up-down asymmetry of the flux surfaces on the turbulent energy input into the GAM in local edge-turbulence computations using single-null geometry. We use the same parameters as in Sec. III. The flux surface is constructed with the magnetic field of five toroidal current loops representing the plasma current and the currents in the shaping coils.[14] The poloidal flux is $\Psi = \sum_i A_i = 0.999\Psi_{sep}$, where $A_i = a_i/2 \ln((R_a + r_i)^2 + (Z + z_i)^2)$ and Ψ_{sep} is the poloidal flux at the separatrix. The coefficients a_i, z_i, and r_i measure the current of conductor i, its position
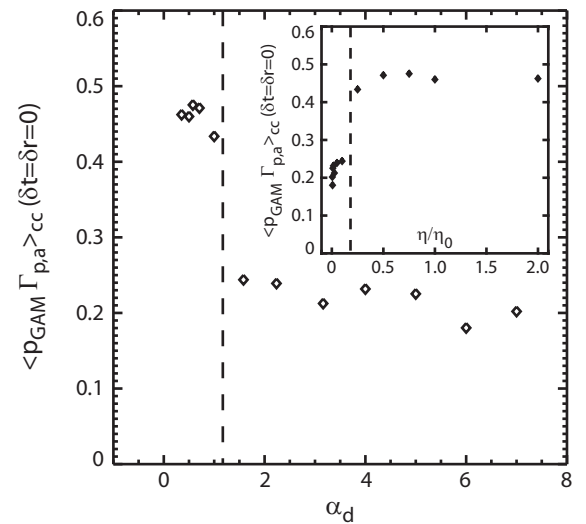

FIG. 5. Cross correlation between the GAM induced pressure perturbations p_{GAM} and the up-down antisymmetric component of the turbulent pressure transport plotted against the parameter α_d and the relative parallel resistivity η/η_0 (inset), where η_0 is the parallel resistivity at $\alpha_d = 0.5$. The dashed lines indicate the transition between a high and a low correlation regime possibly caused by a transition between ITG and resistive ballooning dominated turbulence.

on the (vertical) Z-axis, and its radial position. The radius of the magnetic axis is R_a. For consistency, the coefficients are chosen such that the forces on the plasma current exerted by the four shaping coils add to zero, i.e., $\sum_i a_i/(r_i^2 + z_i^2)^{1/2} = 0$. We choose $r_0 = z_0 = 0$, $a_0 = 1$, $r_1 = 0$, $z_1 = m$, $a_1 = -m$, $r_2 = -r_3 = z_2 = z_3 = m/\sqrt{2}$, $a_2 = a_3 = \sqrt{2}m$, $r_4 = 0$, $z_4 = -1$, and $a_4 = 1$ with $m = 2$ for lower ($z_i \rightarrow -z_i$ for upper) X-point configuration. The ion curvature and ∇B-drifts are directed in the positive Z-direction. In local turbulence runs, the system saturates in both configurations, upper and lower X-point, by exciting GAMs. However, a striking difference is the asymmetry of the nonlinear GAM drive with respect to the sign of the phase velocity of the GAM, which is obvious in the $\mathbf{E} \times \mathbf{B}$-flow profiles in Fig. 6(a). Only GAMs with radially outward phase velocity are excited with the curvature drift directed away from the X-point, whereas the phase velocity is radially inward with the curvature drift directed towards the X-point. The characteristic radial scale length of the GAMs is the same in both cases. The corresponding (k_r, ω)-spectra reveal that the GAM activity is concentrated close to the linear dispersion. Since the linear group velocity of the GAM in single-null configuration is in direction of the ion curvature drift at a location opposite to the X-point,[14] one can say that GAMs are excited such that the phase velocity is in direction of the group velocity. Including the parameter variation ($\lambda \approx 200$), the GAM flow amplitude and the turbulence

FIG. 7. Flux-surface averaged poloidal $\mathbf{E} \times \mathbf{B}$ flow similar to Fig. 6(b). The time interval covers the initial phase and the first GAM burst.

intensity become correlated and pulsed at a frequency much smaller than the GAM frequency [Fig. 6(b)]. Detailed analysis of the poloidal flow shows that the characteristic radial scale $k_{r,i}$ of the GAM in the initial phase ($t < 100$) is the same as in the local studies. The phase velocity is negative. However, due to the frequency gradient the wave fronts of the flows are being tilted in the r–t-plane and k_r decreases. The tilting is shown in Fig. 7. In response, the GAM-turbulence equilibrium readjusts itself towards transport levels even higher than in computations with artificially suppressed zonal flows. A corresponding intensity plot indicating the dominant wave number of the GAM activity in the region $50 < r < 140$ is shown in Fig. 8(a). At $k_r = 0$, the GAM and turbulence intensity reach a maximum and then drop for $k_r > 0$ as the GAM is damped. After this burst, the described cycle repeats. The pulse frequency obviously depends on the GAM frequency gradient and on the initially growing wave number, i.e., $\omega_b \approx 2\pi/(k_{r,i}\rho_s)\partial_r\omega_{GAM,0}(r)$. A range of $\omega_b \approx 0.01 \ldots 0.5\omega_{GAM}$ seems to be readily realizable by adjusting $\partial_r\omega_{GAM,0}(r)$ and assuming $k_{r,i}\rho_s \sim 0.1$. For opposite sign of the ion curvature drift, the GAM wave number is restricted to $k_r > k_{r,i}$. In this case, the response of the turbulence intensity on the GAM wave number turns out to be weak, and the pulsing is subdominant.

In order to understand the pulsed GAM activity, we investigate the dependence of the GAM-turbulence interaction on the
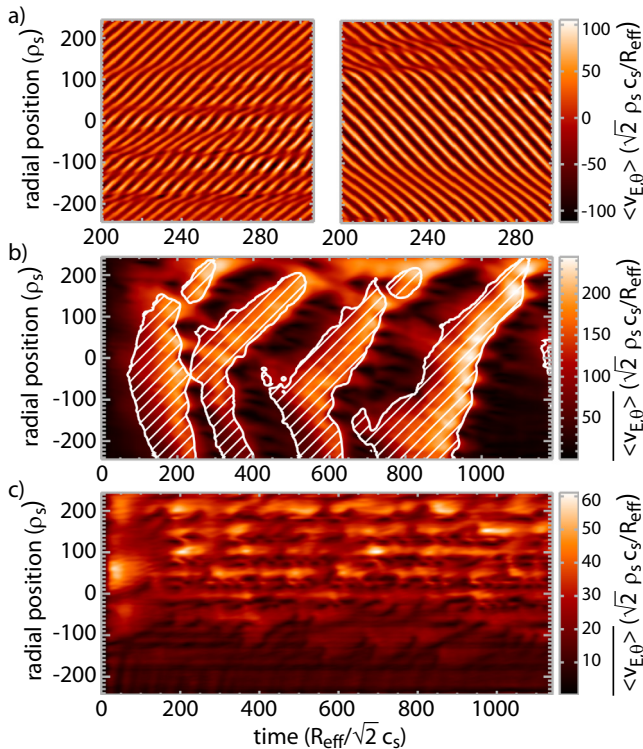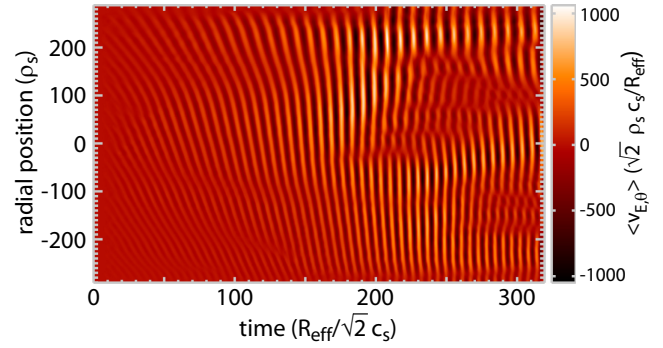

FIG. 6. Flux-surface averaged poloidal $\mathbf{E} \times \mathbf{B}$ flows $\langle v_{E,\theta} \rangle$ of NLET turbulence studies using the same parameters as in Fig. 1 but with a single-null geometry. (a) Local run. Left: Ion magnetic inhomogeneity drift $\mathbf{v}_d$ directed away from the X-point. Right: $\mathbf{v}_d$ directed towards the X-point. (b) Non-local run with $\lambda \approx 200$ and $\mathbf{v}_d$ towards the X-point. Color-coded: short-time-RMS of $\langle v_{E,\theta} \rangle$. Contours: turbulence intensity. Within the shaded areas, the turbulence intensity is above 70% of its RMS average. (c) Like (b) but with opposite $\mathbf{v}_d$. Reprinted with permission from R. Hager and K. Hallatschek, Phys. Rev. Lett. **108**, 035004 (2012). Copyright © 2012 American Physical Society.
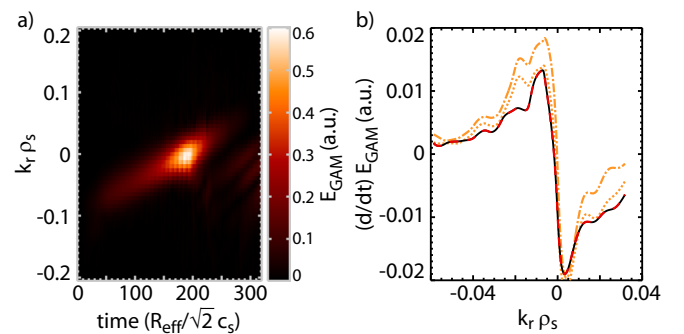

FIG. 8. (a) GAM intensity vs. radial wave number and time corresponding to the region $50 < r < 140$ in Fig. 7. (b) Time derivative of GAM energy (solid, black), energy transfer due turbulent transport (dashed-dotted, orange), the latter with the numerical error added (dotted, orange), and the sum of all energy transfer terms and the numerical error (dashed, red) plotted versus the dominant radial wave number of GAM [as determined from the maximum of the GAM intensity in (a) at each time step].

sign of the phase velocity on the basis of Eq. (11). Since the Reynolds stress and $s_{dia,\phi}$ turned out not to be important for the present parameters, we drop both terms. With $v_{GAM} \approx -i\,(\omega_{GAM,0}/\omega_{GAM})p_{GAM}$, where $\omega_{GAM,0}$ is the linear, ω_{GAM} the (complex) nonlinear GAM frequency, Eq. (11) yields

$$\omega^2 p_{GAM} = p_{GAM} - \partial_t s_\Gamma - \partial_t s_{dia}. \qquad (17)$$

Moreover, we approximate

$$s_{dia,p} \equiv \langle \alpha_\tau \partial_r (p_i + \beta_\tau T_i) \rangle \approx \alpha_\tau \partial_r \langle p \rangle, \qquad (18)$$

where $\alpha_\tau \equiv \tau/(1+\tau)$, $\beta_\tau = \gamma\tau/(1+\gamma\tau)$, and the ion pressure $p_i \equiv n + T_i$, because the temperature in the diamagnetic source term does not change the result qualitatively. Therefore, we may use $\partial_t \langle p \rangle \approx -\partial_r \langle \Gamma \rangle$. The source term due to the turbulent transport Γ can be written as $s_\Gamma = -\partial_r \langle \tilde{C}\Gamma_p \rangle$. The transport itself is expressed as $\Gamma_p = \Gamma_{p,1} + \Gamma_{p,2}$, where $\Gamma_{p,1} \approx \hat{\Gamma}_{p,1}(\theta)(1 - \tau_{dc}\partial_t)v_{GAM}$ describes the modulation of the turbulence intensity due to a poloidal shear flow (for details and the Galilei invariance of this term see Ref. 9), and $\Gamma_{p,2} \approx \hat{\Gamma}_{p,2}(\theta)(1 - \tau_{dc}\partial_t)\partial_r v_{GAM}$ is a correction to $\Gamma_{p,1}$.[4,9] Here, τ_{dc} represents the turbulence decorrelation time, which sets the time scale for the reaction of the turbulence to changes of the shear flow. The poloidal structure of Γ_i is contained in the function $\hat{\Gamma}_{p,i}(\theta)$. Finally, we expand $\omega = \omega_{GAM,0} + \sum_j \epsilon^j (\omega_r^{(j)} + i\omega_i^{(j)})$ and apply the ordering principle $k_r \sim \varepsilon$ in order to obtain from Eq. (17) the turbulence induced frequency shifts and growth rates

$$\omega_r = \frac{k_r}{2}\tau_{dc}\langle \tilde{C}\hat{\Gamma}_{p,1}\rangle_p + \frac{k_r^2}{8}\Big((1 + \tau_{dc}^2)\langle \tilde{C}\hat{\Gamma}_{p,1}\rangle_p^2$$
$$+ 4\langle \tilde{C}\hat{\Gamma}_{p,2}\rangle_p - 4\alpha_\tau\tau_{dc}\langle \hat{\Gamma}_{p,1}\rangle_p \Big) + O(k_r^3), \qquad (19)$$

$$\omega_i = -\frac{k_r}{2}\langle \tilde{C}\hat{\Gamma}_{p,1}\rangle + \frac{k_r^2}{2}\Big(\tau_{dc}\langle \tilde{C}\hat{\Gamma}_{p,2}\rangle_p - \alpha_\tau\langle \hat{\Gamma}_{p,1}\rangle_p \Big) + O(k_r^3). \qquad (20)$$

Only the term linear in k_r in Eq. (20), which originates from s_Γ, can be responsible for the asymmetry of the phase velocity of the turbulent GAM excitation. In up-down symmetric magnetic geometries, $\tilde{C}(\theta)$ is up-down antisymmetric (e.g., $\sin(\theta)/\sqrt{2}$ for circular flux surfaces). Since empirically $\Gamma_{p,1}$ is approximately symmetric with respect to the outboard midplane of the tokamak and positive, $\langle \tilde{C}\hat{\Gamma}_{p,1}\rangle = 0$ and the related growth rate is zero. However, in single-null geometry, $\tilde{C}(\theta)$ becomes very small close to the X-point. Hence, $\langle \tilde{C}\hat{\Gamma}_{p,1}\rangle \neq 0$ and an asymmetry in the phase velocity can arise in Eq. (20). With $\mathbf{b} \times \nabla \ln B$ (the direction of ion magnetic drifts) directed upwards—as is convention in NLET— and upper (lower) single-null geometry, $\tilde{C}(\theta)$ is positive (negative) opposite to the X-point. Thus, $\langle \tilde{C}\hat{\Gamma}_{p,1}\rangle$ becomes positive (negative), and the sign of the asymmetric growth rate $-(k_r/2)\langle \tilde{C}\hat{\Gamma}_{p,1}\rangle$ agrees with the GAM properties observed in Fig. 6(a). Regarding the discussion in Sec. III, note also that Eq. (19) contains a frequency shift due to the asymmetric transport $\delta\omega_{GAM} \propto k_r^2\langle C\hat{\Gamma}_{p,2}\rangle$ which is positive because both, $C(\theta)$ and $\hat{\Gamma}_{p,2}(\theta)$, are negative (positive) above (below) the outboard midplane.[4]

The nonlinear energy transfer between GAMs and the turbulence is analyzed by means of the method developed in Sec. II A. The time derivative of the GAM energy corresponding to the flow profile in Fig. 7 at $r = 95$ is plotted vs. the dominant radial wave number of the GAM in Fig. 8(b) together with the energy transfer due to the transport term s_Γ in Eq. (11). The time interval covered by Fig. 8(b) is centered around the burst shown in Fig. 7, and the radial wave number is determined by the maximum of the GAM intensity in Fig. 8(a) at each time step. While the other energy transfer terms fluctuate around 0 and contribute little to the total energy transfer, the energy transfer due to s_Γ largely reproduces $\partial_t E_G$. As a measure for the numerical error, we calculated the difference between $\partial_t v_{GAM}$ and $\partial_t p_{GAM}$, which are output by NLET, and the corresponding reconstructions $-p_{GAM} + s_\Pi + s_{dia,\phi}$ and $v_{GAM} + s_\Gamma + s_{dia,p}$. The resulting errors are then splitted into errors of the energy transfers and frequency shifts. Including the errors, the energy transfer due to s_Γ is close to $\partial_t E_G$. The sum of all the nonlinear energy transfers and the numerical error reproduce $\partial_t E_G$ exactly. One can therefore safely conclude that the observed nonlinear effect is caused by the turbulent transport as in case of the nonlinear dispersion relation in Sec. III.

V. SUMMARY AND CONCLUSIONS

Compared to linear predictions, numerical ITG turbulence studies display strongly enhanced GAM dispersion in case of non-adiabatic electron response with a dependence on the parallel resistivity. The interaction with the turbulence can raise the group velocity of the GAM from the order of the curvature drift velocity (~ 0.1 km/s, $T \sim 100$ eV, $B \sim 1$ T, $R \sim 1$ m) in the linear case[13,14] to the order of the diamagnetic drift velocity (~ 1 km/s), which is the typical scale of turbulent motions. A global nonlinear eigenmode can be wide enough to form frequency plateaus as observed in ASDEX Upgrade.[15] Since the group velocity determines the flux of the energy stored in the GAM and the width of its resonance regions, fast propagation might also play a role in considerations about the efficiency of externally driven GAMs as transport barriers. Moreover, taking into account the propagation properties close to the separatrix discussed here and in Refs. 13 and 14 in addition to the high group velocities, one might also speculate about trapping the GAM between two reflection layers. Thus, an enhanced GAM drive efficiency might assist the L-H transition.

Up-down asymmetry of the magnetic configuration results in an additional GAM growth rate causing a preference for one particular sign of the phase velocity. In NLET runs using single-null geometry with the ion curvature drift directed upwards and upper (lower) X-point this interaction favors the excitation of GAMs with negative (positive) group and phase velocities. Taking into account a radial frequency gradient, the phase velocity preference results in a pulsed activity of turbulence and GAMs for upper X-point. In contrast, for lower X-point pulsing is subdominant and the turbulence saturates into a quasi-steady state with the mean turbulence intensity being significantly lower than for upper X-point.

Since the only ingredients necessary to obtain pulsed GAM activity in our two-fluid computations are non-locality

and up-down asymmetric flux surfaces, the underlying mechanism might serve as an explanation for GAM intermittency in many situations. For example, the pulsed GAM activity reported here displays some similarity to observations during the I phase in ASDEX Upgrade,[2] where GAM activity is reported to coincide with time intervals of enhanced turbulence activity. The mechanism discussed in Sec. IV might also be involved in the explanation of the quiet periods in NSTX.[17] Since the ion curvature drift was directed towards the X-point in all of the discharges analyzed in Ref. 17, it would be interesting to investigate the changes related to an inversion of the curvature drift in the experiment. However, one has to keep in mind that not all effects which may become important in plasma tokamak edge can be retained in our two-fluid turbulence computations.

ACKNOWLEDGMENTS

[1]N. Winsor, J. L. Johnson, and J. M. Dawson, "Geodesic acoustic waves in hydromagnetic systems," Phys. Fluids **11**, 2448 (1968).

[2]G. D. Conway, C. Angioni, F. Ryter, P. Sauter, J. Vicente, and ASDEX Upgrade Team, "Mean and oscillating plasma flows and turbulence interactions during the L-H confinement transition," Phys. Rev. Lett. **106**, 065001 (2011).

[3]E. J. Kim and P. H. Diamond, "Zonal flows and transient dynamics of the L-H transition," Phys. Rev. Lett. **90**, 185006 (2003).

[4]K. Itoh and S.-I. Itoh, "Excitation of geodesic acoustic mode in toroidal plasmas," Plasma Phys. Controlled Fusion **47**, 451 (2005).

[5]K. Itoh, Y. Nagashima, S.-I. Itoh, P. H. Diamond, A. Fujisawa, M. Yagi, and A. Fukuyama, "On the bicoherence analysis of plasma turbulence," Phys. Plasmas **12**, 102301 (2005).

[6]T. Lan, A. D. Liu, C. X. Yu, L. W. Yan, W. Y. Hong, K. J. Zhao, J. Q. Dong, J. Qian, J. Cheng, D. L. Yu, and Q. W. Yang, "Spectral features of the geodesic acoustic mode and its interaction with turbulence in a tokamak plasma," Phys. Plasmas **15**, 056105 (2008).

[7]N. Chakrabarti, R. Singh, P. K. Kaw, and P. N. Guzdar, "Nonlinear excitation of geodesic acoustic modes by drift waves," Phys. Plasmas **14**, 052308 (2007).

[8]N. Miyato, Y. Kishimoto, and J. Li, "Global structure of zonal flow and electromagnetic ion temperature gradient driven turbulence in tokamak plasmas," Phys. Plasmas **11**, 5557 (2004).

[9]K. Hallatschek and D. Biskamp, "Transport control by coherent zonal flows in the core/edge transitional regime," Phys. Rev. Lett. **86**, 1223 (2001).

[10]R. Hager and K. Hallatschek, "Nonlinear dispersion relation of geodesic acoustic modes," Phys. Rev. Lett. **108**, 035004 (2012).

[11]K. Hallatschek and A. Zeiler, "Nonlocal simulation of the transition from ballooning to ion temperature gradient mode turbulence in the tokamak edge," Phys. Plasmas **7**, 2554 (2000).

[12]K. Itoh, S.-I. Itoh, P. H. Diamond, A. Fujisawa, M. Yagi, T. Watari, Y. Nagashima, and A. Fukuyama, "Geodesic acoustic eigenmodes," Plasma Fusion Res. **1**, 037 (2006).

[13]R. Hager and K. Hallatschek, "Radial propagation of geodesic acoustic modes," Phys. Plasmas **16**, 072503 (2009).

[14]R. Hager and K. Hallatschek, "Radial propagation of geodesic acoustic modes in up-down asymmetric magnetic geometries," Phys. Plasmas **17**, 032112 (2010).

[15]G. D. Conway, C. Troster, B. Scott, K. Hallatschek, and ASDEX Upgrade Team, "Frequency scaling and localization of geodesic acoustic modes in ASDEX Upgrade," Plasma Phys. Controlled Fusion **50**, 055009 (2008).

[16]J. C. Hillesheim, W. A. Peebles, T. A. Carter, L. Schmitz, and T. L. Rhodes, "Experimental investigation of geodesic acoustic mode spatial structure, intermittency, and interaction with turbulence in the diii-d tokamak," Phys. Plasmas **19**, 022301 (2012).

[17]S. J. Zweben, R. J. Maqueda, R. Hager, K. Hallatschek, S. M. Kaye, T. Munsat, F. M. Poli, A. L. Roquemore, Y. Sechrest, and D. P. Stotler, "Quiet periods in edge turbulence preceding the L-H transition in the National Spherical Torus Experiment," Phys. Plasmas **17**, 102502 (2010).

[18]H. Sugama and T.-H. Watanabe, "Collisionless damping of geodesic acoustic modes," J. Plasma Phys. **72**, 825 (2006).

[19]J. Candy and R. E. Waltz, "An eulerian gyrokinetic-Maxwell solver," J. Comput. Phys. **186**, 545 (2003).

[20]A. Zeiler, D. Biskamp, J. F. Drake, and B. Rogers, "Transition from resistive ballooning to η_i driven turbulence in tokamaks," Phys. Plasmas **5**, 2654 (1998).